



Assessment of the correlation between optical properties and CQD preparation approaches

Ebtesam E. Ateia, Obaida Rabie^a , Amira T. Mohamed

Physics Department, Faculty of Science, Cairo University, Giza, Egypt

Received: 13 August 2023 / Accepted: 19 December 2023
© The Author(s) 2024

Abstract Various production procedures, for carbon quantum dots (CQDs), are still being extensively researched to understand the nature of CQD luminescence. This study compares and examines the impact of chemical as well as green methods on the structural and optical properties of CQDs. We present a straightforward, cost-effective bottom-up method for producing fluorescent CQDs from lemon peels (L-CQDs), orange juice (O-CQDs), and citric acid (C-CQDs) without having to deal with time-consuming or ineffective post-processing processes. The proposed green synthesis has no toxic by-products, and the residual resources utilized promote the large-scale production of CQDs. X-ray diffraction, high-resolution transmission electron microscopy, FTIR, Raman, DLS, and UV–Vis spectroscopy are utilized to investigate the structure and optical characteristics of the prepared CQDs. The as-prepared CQDs possess small particle sizes of 5.6 nm, 6.2 nm, and 1.1 nm for L-CQDs, O-CQDs, and C-CQDs samples, respectively. FTIR results reveal the coexistence of carboxylic and hydroxyl groups on the surface of the CQDs, as also supported by zeta-potential values. Maximal fluorescence intensity was reached at excitation wavelengths of 365, 250, and 280 nm with an emission color of blue, indigo, and light blue for L-CQDs, O-CQDs, and C-CQDs, respectively. The presented approaches show a high quantum yield of 88% for O-CQDs, 49% for L-CQDs, and 37% for C-CQDs. Due to their minuscule particle size, perfect water solubility, high stability, and tunable luminescence properties, the prepared CQDs are preferred for potential applications in multicolor imaging, metal ion sensing, and wastewater technologies.

1 Introduction

Fluorescent size-dependent semiconductor spherical nanocrystals with sizes between 1 and 10 nm with profuse surface chemistry and unrivaled optical properties are called quantum dots (QDs). The well-known semiconductor QDs based on metallic elements, such as PbSe, CdSe, and Ag₂S face the drawbacks of high cost, toxicity, and hydrophobicity, which restrict their practical applicability [1–3]. Carbon dots are a newly discovered class of carbon-based nano materials. They were found during the purification of single-walled carbon nanotubes, which have garnered significant attention for their potential in promoting efficient energy conversion through a reliable and environmentally friendly approach [4]. Due to their minuscule particle size, perfect water solubility, high stability, and tunable luminescence properties, the prepared CQDs are highly recommended for use in multicolor imaging, metal ion sensing, and wastewater technologies. Future research should focus on investigating the prepared CQDs in these applications [5].

Common obstacles in multicolor imaging with CQDs include the potential overlap of emission spectra, especially when using different-sized or chemically modified CQDs. This can make it difficult to distinguish between different colors or obtain clear and distinct images. One strategy to overcome this obstacle is to engineer and tune the emission wavelengths of the CQDs. This can be achieved by precisely controlling the size, composition, and surface functionalization of the CQDs, as well as by varying synthesis parameters such as reaction time, temperature, and precursor concentration. By carefully selecting and optimizing the CQDs used in multicolor imaging, it becomes possible to minimize spectral overlap and achieve distinct emission colors [6–8].

To improve the quantum yield or manipulate the emission color of CQDs, there are numerous potential approaches for further adjustment. These may involve adjusting the precursor composition, modifying the surface functional groups, altering reaction conditions such as temperature and time, controlling the density and type of surface defects in CQDs, changing surface passivation, introducing heteroatoms or dopants, or utilizing post-synthesis treatments. These techniques can be utilized to optimize the characteristics of CQDs, including quantum yield and emission color, to meet specific requirements. However, it is important to recognize that the precise tuning methods may vary depending on the type of CQDs and the desired outcome [9–11].

On the other hand, there are potential modifications and functionalization that can enhance the stability of carbon quantum dots (CQDs) for long-term applications. Some strategies that can be used include applying appropriate surface inorganic coatings, organic

^a e-mail: 201527144@std.sci.cu.edu.eg (corresponding author)

ligands, and chemical moieties [9]. Additionally, using appropriate cross-linkers or linking agents can also improve their stability. Another approach to enhance the stability of CQDs is to encapsulate them within protective matrices or materials [12].

Using natural resources for the synthesis of CQDs is not only cost-effective but also environmentally friendly. Green synthesis methods are considered more acceptable compared to physical and chemical procedures. Additionally, CQDs can be produced from a variety of organic waste products. The researchers were inspired to develop a new approach due to the abundance of easily accessible carbon sources in nature. Green synthesis approaches aim to minimize the use of hazardous chemicals, reduce energy consumption, and promote environmental sustainability. Although they have numerous eco-friendly benefits, it is essential to assess their potential for scalability. Factors such as the availability of natural and/or renewable resources, cost-effectiveness, accessibility of raw materials, and a reasonable timeframe are crucial for facilitating large-scale production. Additionally, the ability to achieve a high yield of CQDs per batch, and the lack of need for extensive equipment and infrastructure make their implementation on a larger-scale feasible [13, 14].

In comparison to standard methods, green methods offer a more sustainable approach avoiding the use of harsh chemicals, high temperatures, and energy-intensive processes. Standard methods can result in pollution, resource depletion, and health risks [15]. Additionally, they may have limitations in terms of economical and large-scale production due to their harsh synthesis conditions, complex processes, and low production yields. Green methods address ecological challenges such as resource availability and sustainability, waste management and disposal, chemical substitution and toxicity, and time restrictions that need attention and resolution [16].

The procedures for synthesizing CQDs are traditionally divided into two categories, “top-down” and “bottom-up” synthesis. Top-down approaches employ techniques including arc discharge, laser ablation, and electrochemical methods to break down carbon material into carbon nanoparticles (CNPs). On the other hand, bottom-up schemes involve surface passivation in a single-pot synthesis with no further steps required. These methods include microwave-assisted polymerization, hydrothermal reaction, pyrolysis, and carbonization for turning tiny organic precursors into CQDs [17–19].

Certainly, one of the most well-known bottom-up approaches mentioned above is hydrothermal treatment. This method is utilized to produce CQDs from eco-friendly sources like fruit juices, peels, and plant materials. Typically, an appropriate solvent is used to dissolve tiny organic molecules, and then they are heated to a high temperature (100–200) °C in a Teflon autoclave as part of a standard operation. The tiny organic molecules come together to form carbogenic cores, which eventually grow into CQDs [20].

This study presents a highly effective and simple bottom-up method for the precise preparation of CQDs by adjusting the level of carbonization of a standard organic precursor and citric acid (CA). A comparison was made between three CQD samples. Two of them were prepared using a sustainable approach with orange juice (O-CQDs) and lemon peels (L-CQDs) as the carbon source. The third sample was prepared using a chemical method utilizing citric acid as the carbon source.

2 Experimental work

2.1 Synthesis of CQD samples

The synthesis of carbon quantum dots (CQDs) can vary depending on the specific method employed. However, there are some general characteristics and circumstances commonly used in CQD synthesis. Key aspects include: the use of carbonaceous precursors, carbonization/pyrolysis, reaction conditions, and solvent selection [16, 17]. In this work, water is used as a solvent to minimize the risk of oxidation or degradation. The reaction conditions, including temperature, duration, and precursor concentration are optimized to achieve the desired characteristics and luminescence properties of the synthesized CQDs.

Three samples were prepared using starting materials; lemon peels, orange juice, and citric acid labeled L-CQDs, O-CQDs, and C-CQDs, respectively.

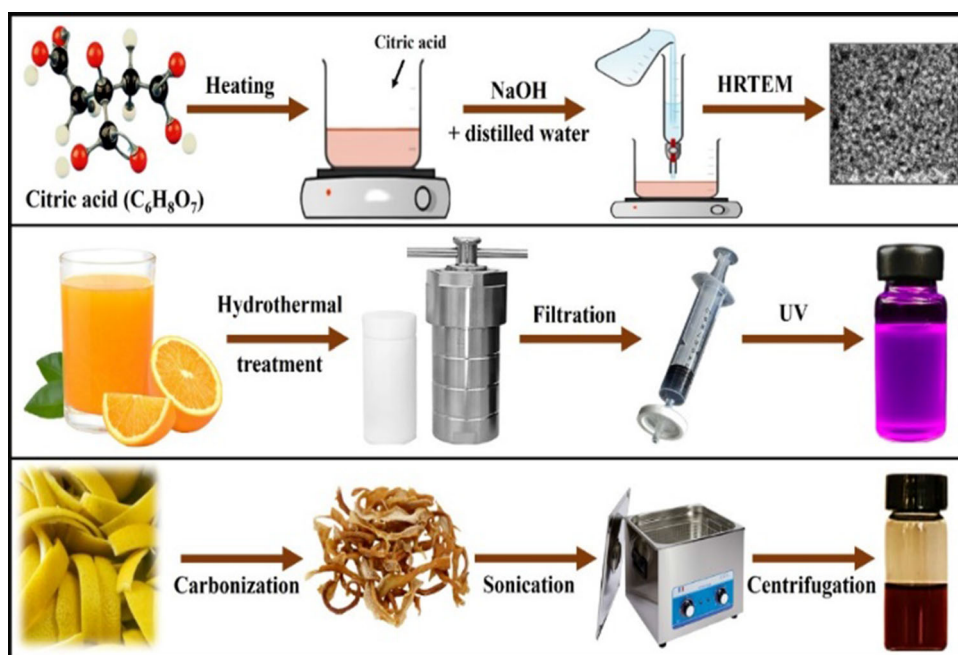
2.1.1 For L-CQDs

Fresh lemon peels were peeled off, then their peels were washed with distilled water, dried, and heated to form homogenous black residues. 2-g powders of black residues were ultrasonically dispersed into 50 mL of distilled water for 1 h. The dispersions were then centrifuged to obtain light-brown residues of L-CQDs (Fig. 1).

2.1.2 For O-CQDs

Fifty milliliter of fresh orange juice was put in a Teflon autoclave and heated at 180 °C for 8 h. Once it has cooled to the ambient temperature, the sample was filtered to obtain fluorescent O-CQDs.

Fig. 1 Schematic illustration of the preparation techniques



2.1.3 For-C-QDs

Two gram of citric acid powder ($C_6H_8O_7$ 99.9%, Fisher chemicals) were heated on the hot plate at $200\text{ }^\circ\text{C}$ for 55 min (until its color changed from white to yellow then finally to orange color). Then, sodium hydroxide solution was added to the citric acid drop by drop until the pH became 7, which indicates the formation of C-CQDs. Schematic illustration of the preparation techniques is presented in Fig. 1

2.2 Characterization techniques

The structure was examined using X-ray diffraction (XRD) with a diffractometer (X'Pert PRO PANalytical, Netherland) of a target $Cu\ K\alpha$ ($k = 1.5418\text{ \AA}$). High-resolution transmission electron microscopy (HRTEM) was utilized to examine the samples' morphology and nanostructure. Raman spectra (RS) were recorded in the range of $1200\text{--}2000\text{ cm}^{-1}$ at ambient temperature ($25\text{ }^\circ\text{C}$) by a Raman spectrometer Horiba LabRam HR Evolution (Horiba, Ltd., UK). The FTIR spectrum CQDs were recorded on a Nicolet FTIR spectrophotometer (Impact-410, Madison, USA). UV-visible absorption spectra of the CQDs were recorded using a UV spectrometer Cary 5000. The fluorescence spectra were recorded using a Cary Eclipse fluorescence spectrophotometer.

3 Results and discussion

3.1 Structural analyses

3.1.1 XRD analysis

According to Tang et al. CQDs have core-shell architectures that are either graphitic crystalline (sp^2) or amorphous (mixed sp^2/sp^3), based on the extent of the occurrence of sp^2 carbon in the core [21].

In order to identify the crystal structure and phase purity, the three carbon dot samples are characterized via XRD technique. On the other hand, amorphous CQDs are devoid of periodic crystal lattice [22], cannot diffract electrons [23], and may exhibit an X-ray diffraction pattern with an amorphous halo that has a peak in the $2\theta = 23.4^\circ\text{--}24.6^\circ$ region [24].

The obtained pattern of the samples reveals a broad peak at about $2\theta = 22^\circ\text{--}25^\circ$, as shown in Fig. 2. The broad and strong characteristic peak at this range is related to the (002) reflection plane of graphite [25, 26]. This demonstrates that carbon dots have poor crystallinity, which is caused by the formation of additional oxygen-containing groups. This is verified by the selected area electron diffraction pattern (SAED) for the amorphous nature and FT-IR for the existence of different oxygen groups [27]. The peaks at 29.3 and 31.8 in the C-CQDs sample may be attributed to insoluble salts during sample handling.

XRD is a vital technique for identifying the crucial characteristics of CQDs with a crystalline structure, but it is inappropriate for describing amorphous CQDs.

Fig. 2 XRD patterns for synthesized CQDs samples

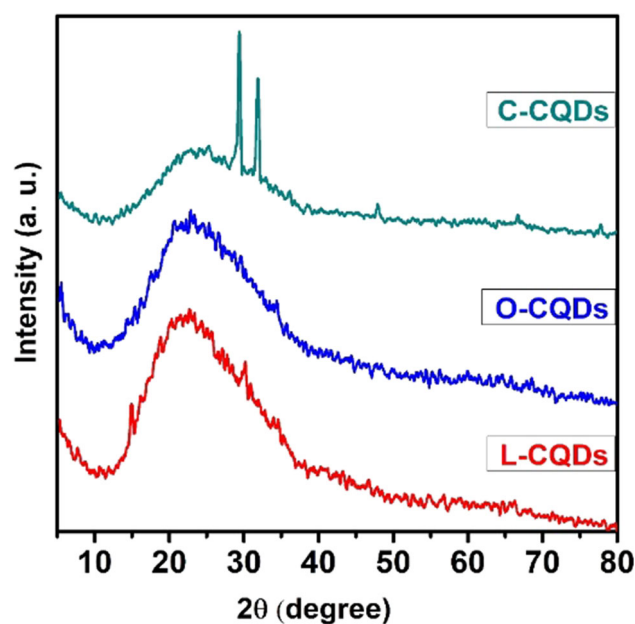
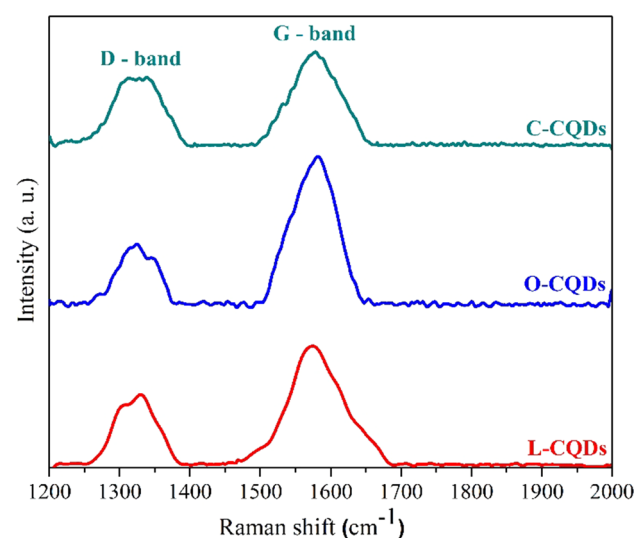


Fig. 3 Raman spectra of L-CQDs, O-CQDs, and C-CQDs

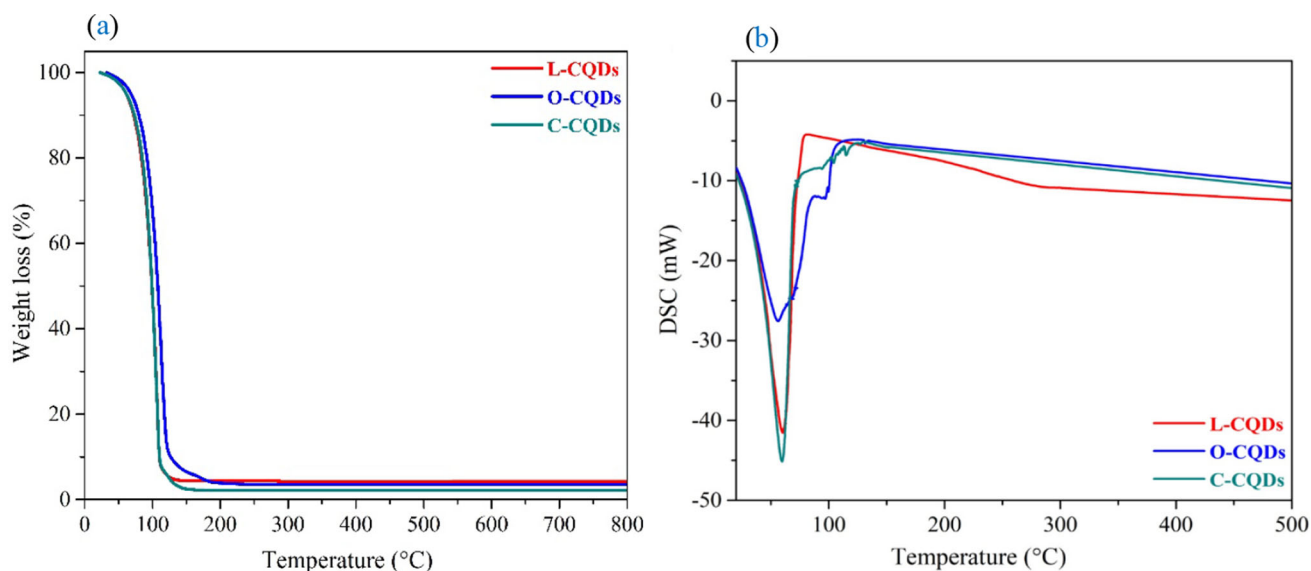
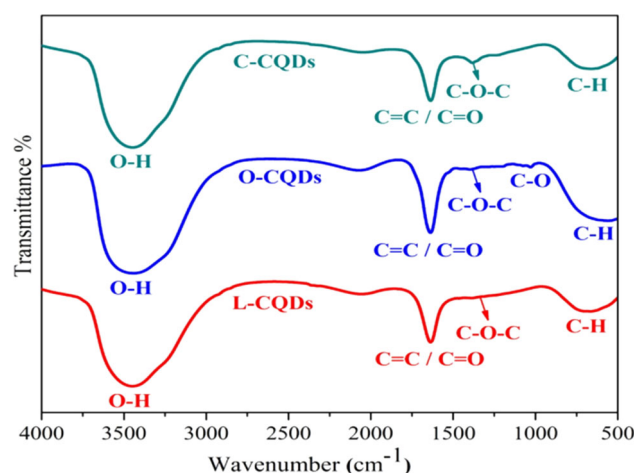


3.1.2 Raman spectroscopy (RS)

RS of the CQDs (Fig. 3) shows two broad peaks in the 1330–1340 and 1575–1582 cm^{-1} ranges, associated with the D band (sp^3 hybridization) and G band (sp^2 hybridization), respectively. The shape of these bands indicates the amorphous nature of the CQDs samples [10], which is consistent with the XRD and HRTEM analyses. The D band is associated with the vibrations of dangling-bond carbon atoms at the edge of the plane of disordered graphite or glassy carbon. The G band correlates to the E_{2g} mode of the graphite and is attributed to the two-dimensional (2D) hexagonal lattice vibration of sp^2 -bonded carbon atoms [28].

3.1.3 FT-IR spectroscopy

The FT-IR technique is utilized to examine the surface structure, functional groups, and linkages in the produced CQDs. The FT-IR spectra are presented in Fig. 4. The strong broadband observed between 3100 and 3440 cm^{-1} is attributed to the O–H stretching vibration [29], which occur as a result of hydrolysis during the reduction process [30]. The band at $\approx 1636 \text{ cm}^{-1}$ can be assigned to the stretching modes of the aromatic hydrocarbons (C=C) and/or oxygenic groups (C=O). The peaks at around 1384 cm^{-1} and 1033 cm^{-1} come from the asymmetric and symmetric stretching vibration of C–O–C and C–O groups, respectively [31, 32]. These observations indicate the presence of carboxylic and hydroxyl groups on the CQDs' surface, as also supported by zeta potential values (to be demonstrated later). Finally, the resulting band in the range of 660–670 cm^{-1} is attributed to C–H bending [29, 33].

Fig. 4 The FT-IR spectra of L-CQDs, O-CQDs, and C-CQDs**Fig. 5** a TGA and b DSC spectra recorded for the investigated samples

It is anticipated that massive quantities of COOH groups present at the CQDs' surface are likely to arise. The CQDs are naturally very hydrophilic due to the presence of C–O–C and C–H functional groups on their surface [34]. The existence of such functional groups demonstrates that the produced CQDs are functionalized with –C–H, C=O, and –OH, which can be employed as linkers to bind therapeutic moieties for the delivery of drugs to diseased cells.

3.1.4 Thermal analyses

The thermal stability of the as-synthesized CQDs was evaluated using a thermogravimetric analyzer (TGA). Figure 5a presents the TGA curves for the three liquid samples heated up to 800 °C. Consistent with prior literature, carbon cores were observed to survive over the entire temperature range [35]. Below, 120 °C, all samples exhibited similar behavior likely due to the desorption of bound water and the degradation of surface groups within the CQDs. The O-CQDs which have more surface groups, experienced a greater alteration in mass.

To determine whether energy is absorbed or released by the liquid CQDs when exposed to high temperatures, DSC analysis is carried out. According to the DSC curves in Fig. 5b, L-CQDs, O-CQDs, and C-CQDs exhibited one endothermic peak. The heat absorption at these temperatures may be attributed to the desorption of bound water molecules found in the liquid CQDs. Up to a temperature of 500 °C, none of the liquid CQDs showed any sign of a peak or thermal deterioration.

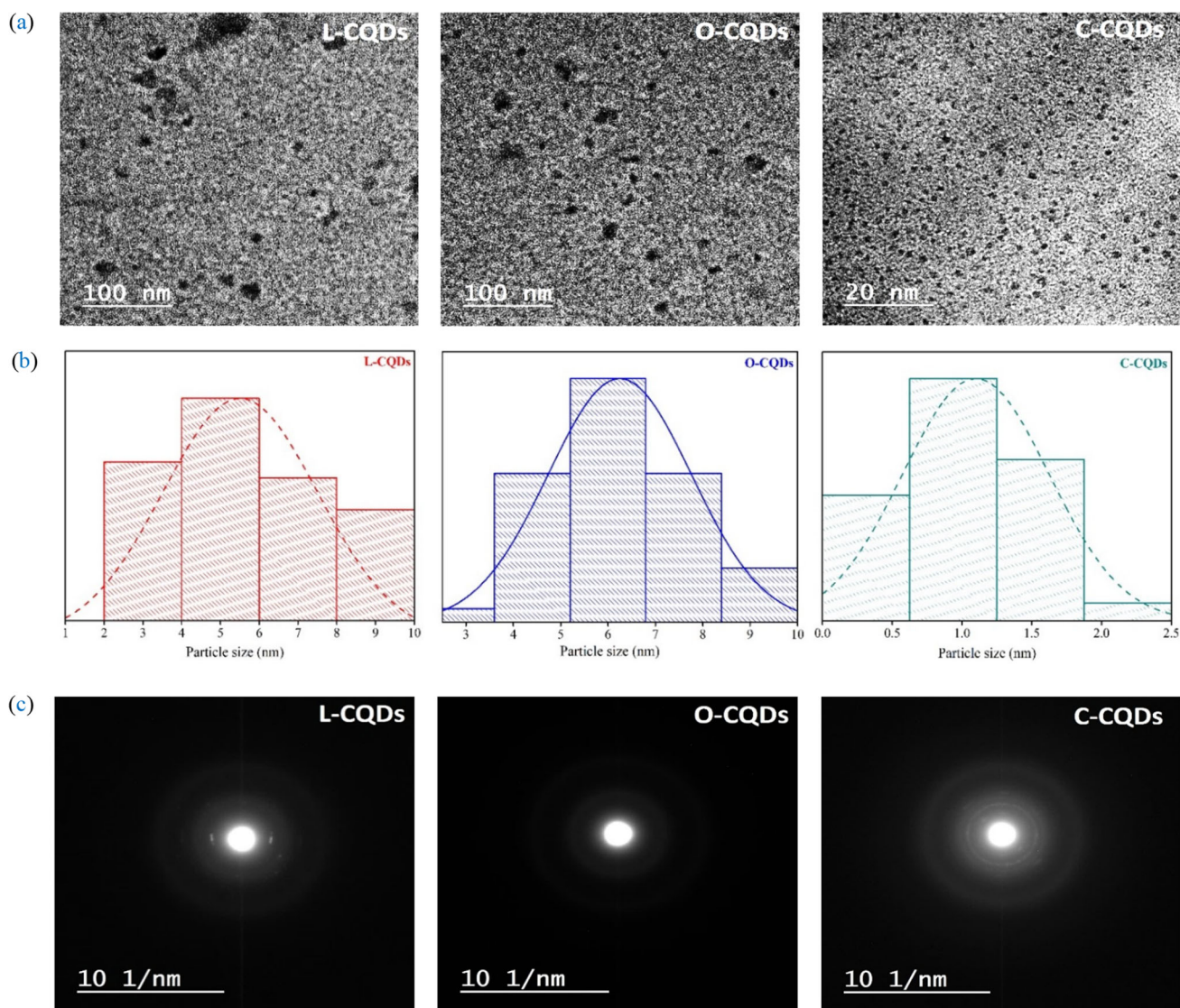


Fig. 6 a HRTEM patterns, b size distribution histograms, and c SAED patterns for L-CQDs, O-CQDs, and C-CQDs

3.2 Morphology

3.2.1 HRTEM

The prepared fluorescent CQDs demonstrate quite highly monodispersed and uniform spherical morphology. These results are consistent with HRTEM images obtained by Cheng et al. [23], which revealed that the CQD particles exist in quasi-zero dimension, with a size distribution ranging from 1 to 10 nm. After measuring of several hundred particles, the particle size distribution of CQDs was determined, showing that the average size of L-CQDs, O-CQDs, and C-CQDs samples is 5.6 nm, 6.2 nm, and 1.1 nm, respectively, as shown in Fig. 6b.

Additionally, Fig. 6c shows the SAED patterns recorded for L-CQDs, O-CQDs, and C-CQDs samples. The concentric rings characteristic of the pattern disappear when the CQD particle sizes are very small or completely amorphous, leaving a halo around the bright center point. This demonstrates that the electrons are scattered randomly by the amorphous structure of the CODs. These results agree well with the result obtained by XRD and Raman spectroscopy.

3.2.2 Zeta potential and DLS analysis

Zeta potential is used to identify the positive or negative charge on the CQDs' surface and the amount of electrostatic contact between them [36, 37]. By using the dynamic light scattering (DLS) technique, the average sizes of the samples are estimated. It

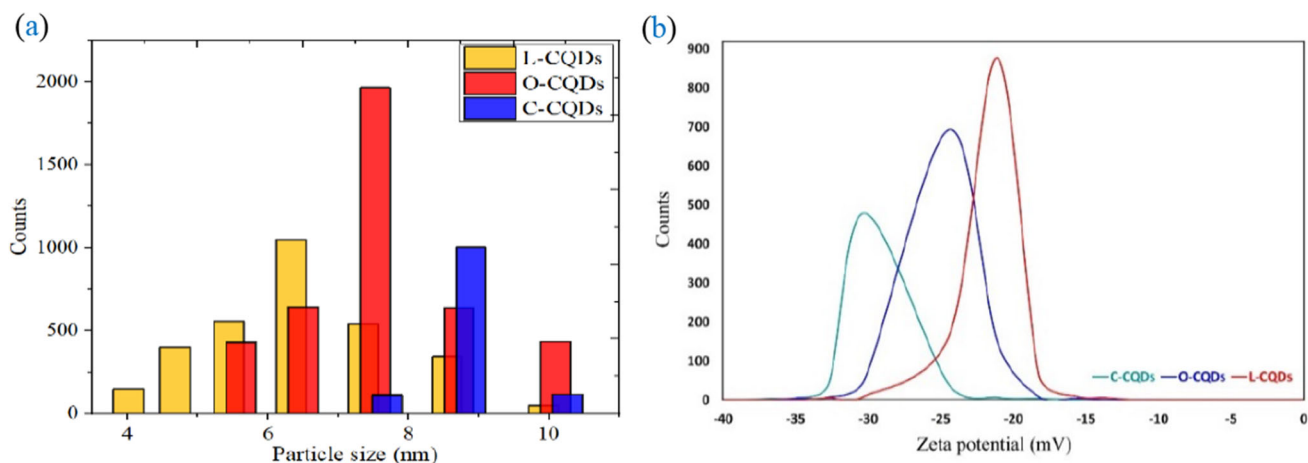


Fig. 7 a DLS size distribution curve and b zeta-potential curve for the prepared CQD samples

was found that, as a result of contamination during sample handling, the average size may be greater than that obtained in HRTEM. In addition, DLS is an intensity-based particle size measurement (large particles are highly sensitive to DLS), whereas HRTEM is a number-based one [38]. The DLS analysis (Fig. 7a) revealed that the average sizes are 6.5, 7.5, and 8.7 nm for LCQDs, O-CQDs, and C-CQDs, respectively, which is consistent with the HR-TEM results.

The magnitude of the zeta potential is an indicator of the potential stability of a colloidal system. According to Sivasankaran et al. [39], the positive and negative signs of the zeta potential reflect the surface charges of nanoparticles (NPs), NPs with a high magnitude of zeta potential (either positive or negative) typically exhibit strong electrostatic repulsion, which prevents them from coming into close contact and aggregating. Higher zeta-potential values indicate greater stability against aggregation.

Using hydrothermal methods, Sachdev et al. [37] isolated CQDs from coriander leaves, and a zeta-potential analyzer was utilized to examine the zeta-potential value. A negative zeta-potential value (-24.9 mV) was observed, which was mainly due to the presence of oxygen-containing functional groups on the CQDs' surface. In this study, the strongly anionic CQDs are defined as those with zeta potentials smaller than -30 mV [40]. Monitoring the zeta potential over time shows no significant changes indicating the stability of CQD dispersions. Additionally, the zeta potential for all investigated samples shows a sharp single peak with negative values of 21.2 mV, 24.4 mV, and 30.1 mV for L-CQDs, O-CQDs, and C-CQDs, respectively (Fig. 7b). The negative potential suggests that the CQDs' surface has negative charge moieties as demonstrated previously in FTIR analysis.

Based on the aforementioned results from XRD, FT-IR, HR-TEM, RS, DLS, zeta potential, and thermal analyses, it can be concluded that the O-CQD has a higher number of surface functional groups, a moderate zeta-potential value, and the largest size compared to the other samples.

3.3 Optical properties

3.3.1 UV-Vis absorption

UV-visible spectroscopy is based on the concept that chemical compounds can absorb ultraviolet or visible light, resulting in distinct spectra. The interaction between light and matter forms the basis of spectroscopy.

In the case of the fluorescent CQD samples, UV-visible spectra (UV-Vis) were measured between 200 and 800 nm. Figure 8a displays absorption peaks in the UV region, with a tail extending into the visible range, indicating the formation of CQDs [41].

The absorption bands in the range of 214–300 nm correspond to an aromatic $\pi-\pi^*$ transition of the C=C bond and the associated electron transitions in the oxygen-containing CQDs.

Additionally, the observed absorption band at 319 nm is attributed to the $n-\pi^*$ transition of the C=O bond (related to the sp^3 carbon system) [42, 43]. These two absorption bands suggest that CQDs possess both conjugated structures and oxygen (O_2) containing functional groups [44].

However, C-CQDs do not have a band above 240 nm (Fig. 8a). The data suggest that fewer functional groups (e.g. COOH) are present on the C-CQD surface, resulting in a larger band gap due to surface passivation [11].

The observed absorption band locations generally vary somewhat depending on the raw precursor and synthesis technique.

3.3.2 Fluorescence analysis

The mechanism of CQD emission is still not fully understood, but the creation of advanced colloidal quantum dots (CQDs) with specific optical properties involves a combination of various factors. These factors include the size of the quantum dots [45], the

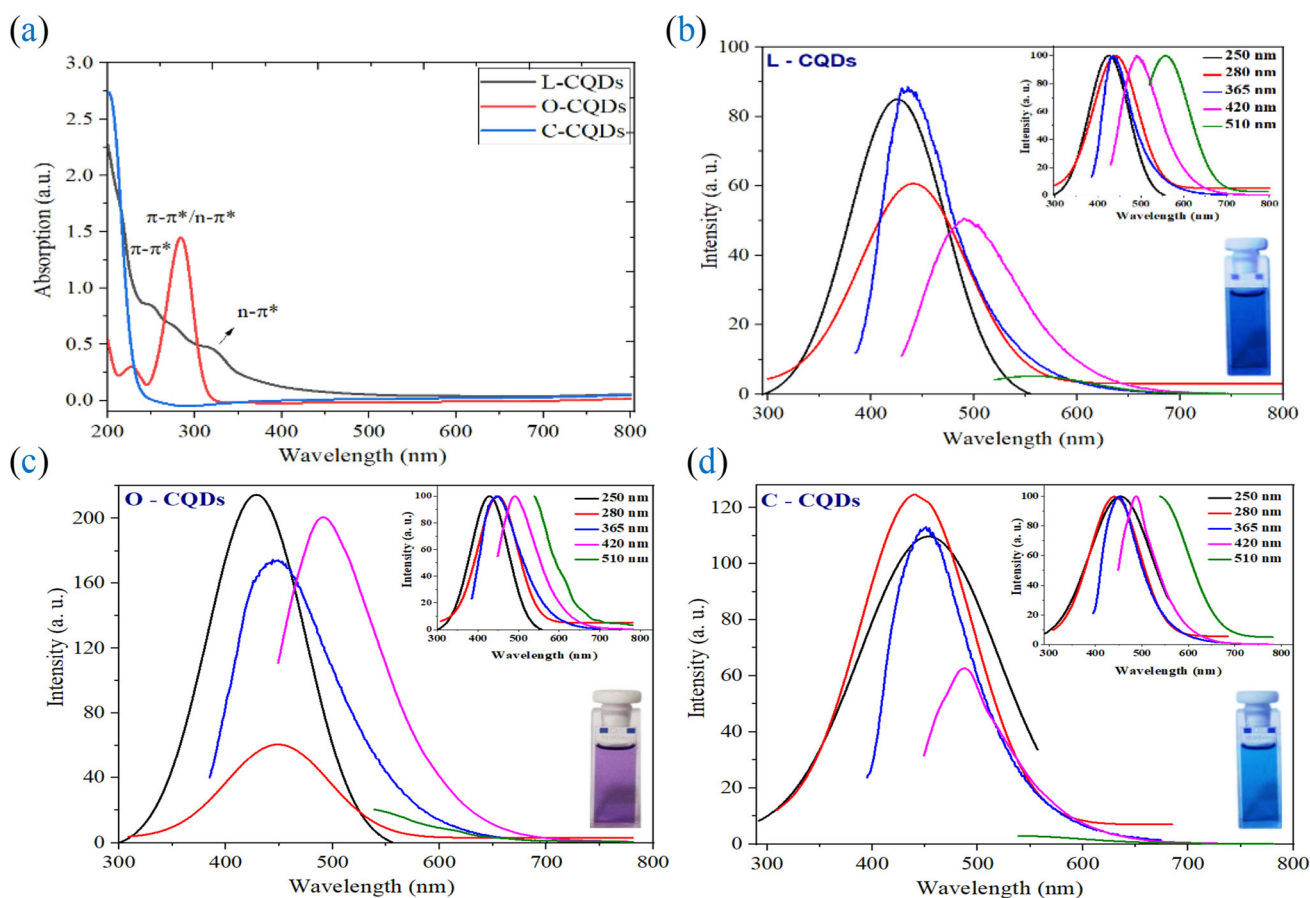


Fig. 8 a Absorption spectra for the investigated samples and **b–d** fluorescence spectra recorded for L-CQDs, O-CQDs, and C-CQDs, respectively

method of preparation, reaction conditions [46], surface passivation [47], atomic doping [48], coating the CQDs with an additional semiconductor layer [49], and surface functionalization of CQDs.

Currently, there are several anticipated theoretical explanations, for the optical characteristics of CQDs including the quantum size effect, the surface state electron–hole radiation rearrangement, and the molecular state luminescence emission mechanism. Previous studies have shown that the regular excitation-based emission spectra of CQDs samples recorded at various excitation wavelengths (250, 280, 365, 420, and 510 nm) demonstrate the distinctive optical characteristics of CQDs [50]. A red shift is observed in the fluorescence spectra from 365 to 510 nm, which may be attributed to the structure with larger conjugation. Interestingly, the intensity of emission peaks is higher in the case of O-CQDs than L-CQDs and C-CQDs.

The maximum intensity occurs at excitation wavelengths of 365, 250, and 280 nm with an emission color of indigo for O-CQDs, blue for L-CQDs, and light blue for C-CQDs (see inset of Fig. 8). The insets of Fig. 8b–d show the normalized intensities of the spectra for different excitation wavelengths.

The generated spectra can exist independently of the carbogenic core or can be connected to it resulting in numerous emitting sites. In this scenario, neither the CQDs core (intrinsic emission) nor the surface functional groups (extrinsic emission) fully govern the emission characteristics.

Additionally, a range of emission colors from indigo to green is observed for an excitation wavelength sweep λ_{ex} from 250 to 510 nm. This tunable multicolor emission phenomenon can be attributed to several molecular-level processes, including a general graphitic carbon core property [51], as well as the quantum confinement effect or energy traps of surface functional groups [52] and various surface defects [53].

The availability of sp^2 sites, the small size of CQDs, and their aromatic conjugated structures may all contribute to the emission properties of CQDs. The photoluminescence property of the prepared CQDs shows promise for various potential applications.

The band gap model provides a good explanation for the majority of optical characteristics of semiconductors [54]. Therefore, the estimation of the band gap is significant in the characterization of materials. Typically, the optical absorption edge energy is used to determine the band gap, which is described as the lowest amount of photon energy necessary to excite an electron from its highest occupied molecular orbital (HOMO, the upper level of the valence band in semiconductor domains) to its lowest occupied molecular orbital (LUMO, the lowermost of the conduction band) [55].

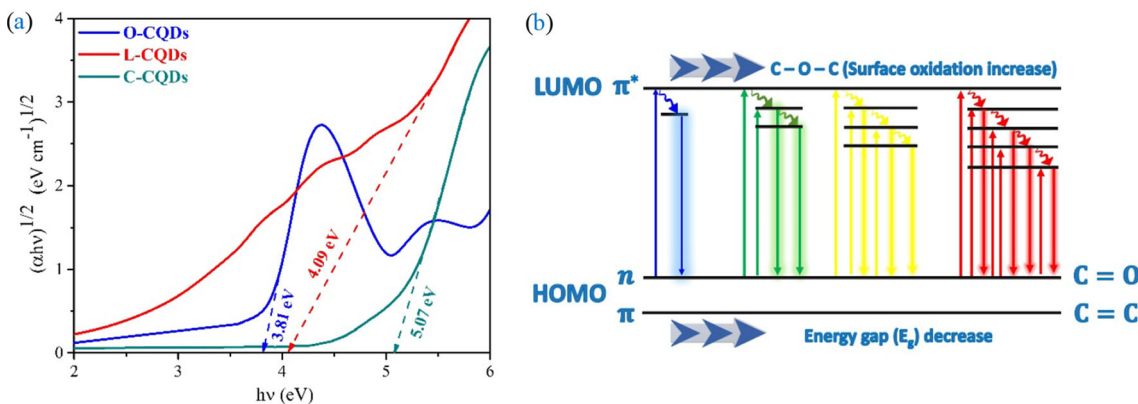


Fig. 9 **a** The energy gap from the plot of $(\alpha hv)^{1/2}$ versus hv and **b** A schematic representation of the energy band structure of the prepared CQDs

Near the absorption edge, the absorption coefficient is expressed as follows:

$$\alpha hv = (hv - E_g)^n \tag{1}$$

where α is the absorption coefficient, hv is the photon energy, and n is a constant that can take different values for different transitions obeying well-defined selection rules. Thus, for permitted direct transition $n = 1/2$, and for permitted indirect transition $n = 2$ [56].

A graph is plotted between $(\alpha hv)^n$ and hv , which is known as (Tauc plot). The straight line’s extrapolation to $(\alpha hv) = 0$ gives the value of energy gap energy [55, 57].

Herein, the value of the energy gap reveals that the fluorescence of CQDs results from surface-state emission (see Fig. 9a). Smaller-sized CQDs generally have a larger surface area-to-volume ratio, which results in a higher density of surface functional groups that can influence their fluorescence characteristics [58]. Based on first-principal calculations of Yan et al. [59], the C–O–C and C–OH groups can induce significant local distortion and then create various energy gaps located in the band tail of the π – π^* gap. With the increase of C–OH and C–O–C groups in CQDs, a large number of localized electronic states are expected to form below the π^* state [60], creating numerous new energy levels between n - π^* gaps (Fig. 9b). More surface traps are present in the O-CQDs sample, and, as a result, the energy levels are constrained.

Therefore, the enhanced absorption intensity of the π – π^*/n - π^* transition in O-CQDs than in L-CQDs is related to its larger number of surface functional groups which undoubtedly contributed to the redshift of absorption peak in Fig. 8a.

When evaluating fluorescent nanomaterials, quantum yield (QY) is a crucial factor to consider. The simplest way to calculate QY is by comparing the sample’s fluorescence intensity to that of a reference compound. It is important that the sample and chosen standard absorb and emit in the same regions. In the case of CQDs and Rhodamine B (RhB), they have similar absorption spectra. Therefore, RhB dissolved in ethanol (ETOH) is used as the reference substance to determine the QY of the CQDs.

The QY of CQDs is calculated via the following equation:

$$QY_s = QY_r \frac{m_s n_s^2}{m_r n_r^2} \tag{2}$$

where the subscripts r and s refer to the reference and sample, respectively, and m is the slope of the integrated fluorescence intensity versus absorbance curve. (see Fig. 10), and n is the refractive index (1.33 for distilled water and 1.36 for ETOH). The QY is 88% for O-CQDs, 49% for L-CQDs and 37% for C-CQDs. Interestingly, the obtained values of QY are higher compared to other previously studied samples, as shown in Table 1.

The high QY fluorophores often produce intense fluorescence. As a result, high-QY material commonly has a variety of applications in the biological, optical, and energy areas. The fluorescent QY of CQDs is crucial for determining whether they can operate as effective illuminating materials for their practical uses. Additionally, one of the important criteria for assessing the optical performance of CQDs, such as in cell imaging, is the quantum yield. The imaging effect is improved with a greater quantum yield value.

Based on the aforementioned, optical results, it follows that by the optimization of the synthesis procedure, it is possible to boost the quantum yield and exert control over the emission color of CQDs.

4 Conclusion

In summary, the influence of the synthesis method on the optical properties of CQDs was examined in the present study. The zeta potential measurement of CQDs provide insightful information on the carbon dots’ aggregation and stability. Based on the results obtained using HRTEM, IR, Raman, and UV–Vis spectroscopy, a series of CQDs with numerous fluorescent colors can be

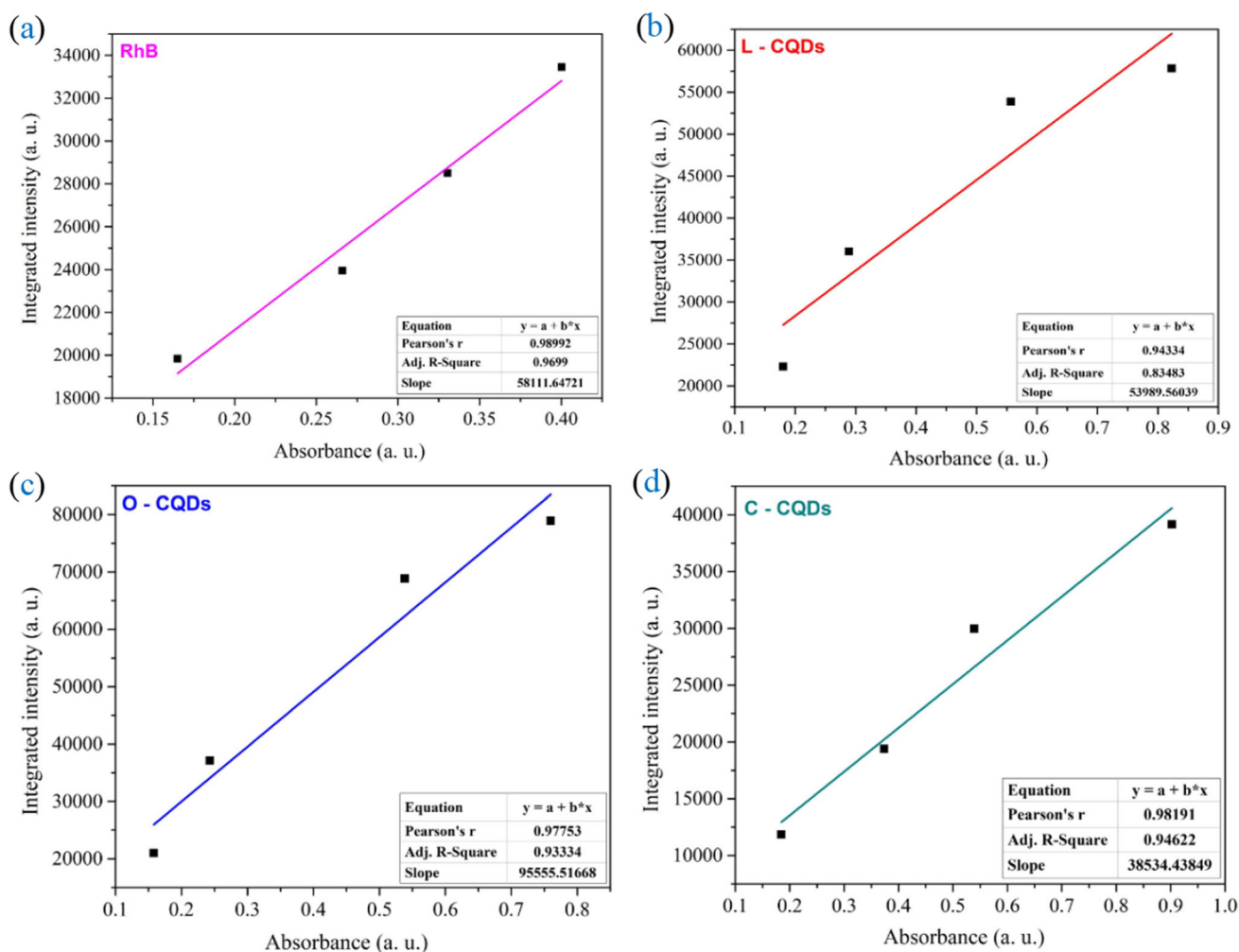


Fig. 10 The dependence of fluorescence intensity on absorption

Table 1 Comparison of the present data and the data reported in the literature

Precursor	Size (nm)	QY (%)	Ref.
Orange juice	0.5–3	31.7	[61]
Lemon peels	1–3	14	[50]
Lemon juice	4.6	28	[62]
Apple juice	2.8	6.4	[63]
Banana peel	5	20	[64]
Ascorbic acid	2.48–3.92	3.22	[65]
Citric acid	6.2	42.5	[66]
	6.5–8.6	51.64	[67]
Lemon peel	5.6	49	The present study
Orange juice	6.2	88	The present study
Citric acid	1.1	37	The present study

manufactured by altering their surface oxidation degree and/or size. The stable CQDs and tunable fluorescence properties with high QY are preferred for potential applications in multicolor imaging, metal ion sensing, and wastewater applications.

5 Future prospects

The production of carbon quantum dots (CQDs) poses various ecological challenges that must be tackled. These challenges encompass waste management, energy consumption, chemical usage, water consumption, and eco toxicity. Addressing these ecological challenges necessitates a multidisciplinary approach involving researchers, industry, and regulatory bodies.

Future efforts will entail a more comprehensive exploration of the molecular-level processes by integrating experimental and computational data. This will enhance our understanding of the adjustable luminescent characteristics of CQDs.

Funding Open access funding provided by The Science, Technology & Innovation Funding Authority (STDF) in cooperation with The Egyptian Knowledge Bank (EKB).

Data Availability Statement All data generated or analyzed during this study are included in this published article.

Declarations

Conflict of interest The authors declare that they have no known competing financial interests or personal relationships that could have appeared to influence the work reported in this paper.

Open Access This article is licensed under a Creative Commons Attribution 4.0 International License, which permits use, sharing, adaptation, distribution and reproduction in any medium or format, as long as you give appropriate credit to the original author(s) and the source, provide a link to the Creative Commons licence, and indicate if changes were made. The images or other third party material in this article are included in the article's Creative Commons licence, unless indicated otherwise in a credit line to the material. If material is not included in the article's Creative Commons licence and your intended use is not permitted by statutory regulation or exceeds the permitted use, you will need to obtain permission directly from the copyright holder. To view a copy of this licence, visit <http://creativecommons.org/licenses/by/4.0/>.

References

1. I. Singh, R. Arora, H. Dhiman, R. Pahwa, Turk. J. Pharm. Sci. **15**, 219 (2018)
2. V. Garg, B.S. Sengar, V. Awasthi, A. Kumar, R. Singh, S. Kumar, C. Mukherjee, V.V. Atuchin, S. Mukherjee, ACS Appl. Mater. Interfaces **10**, 5464 (2018)
3. D.S. Abramkin, M.O. Petrushkov, D.B. Bogomolov, E.A. Emelyanov, M.Y. Yesin, A.V. Vasev, A.A. Bloshkin, E.S. Koptev, M.A. Putyato, V.V. Atuchin, V.V. Preobrazhenskii, Nanomaterials **13**, 910 (2023)
4. P.K. Yadav, S. Chandra, V. Kumar, D. Kumar, S.H. Hasan, Catalysts **13**, 422 (2023)
5. Y. Zhao, L. Yu, Y. Deng, K. Peng, Y. Yu, X. Zeng, Ceram. Int. **49**, 16647 (2023)
6. X. Gao, Y. Cui, R.M. Levenson, L.W.K. Chung, S. Nie, Nat. Biotechnol. **22**, 969 (2004)
7. W. Cai, D.W. Shin, K. Chen, O. Gheysens, Q. Cao, S.X. Wang, S.S. Gambhir, X. Chen, Nano Lett. **6**, 669 (2006)
8. S. Pleskova, E. Mikheeva, E. Gornostaeva, Adv. Exp. Med. Biol. **1048**, 323 (2018)
9. H. Tetsuka, R. Asahi, A. Nagoya, K. Okamoto, I. Tajima, R. Ohta, A.H. OkamotoTetsuka, R. Asahi, A. Nagoya, K. Okamoto, I. Tajima, R. Ohta, A. Okamoto, Adv. Mater. **24**, 5333 (2012)
10. M.A. Omary, H.H. Patterson, Inorg. Chem. **37**, 1060 (1998)
11. A. Laref, N. Alshammari, S. Laref, S.J. Luo, Sol. Energy Mater. Sol. Cells **120**, 622 (2014)
12. M. Gumustas, C. T. Sengel-Turk, A. Gumustas, S. A. Ozkan, B. Uslu, *Multifunctional Systems for Combined Delivery, Biosensing and Diagnostics*, (2017) p. 67
13. Y. Fang, S. Guo, D. Li, C. Zhu, W. Ren, S. Dong, E. Wang, ACS Nano **6**, 400 (2012)
14. H. Li, H. Ming, Y. Liu, H. Yu, X. He, H. Huang, K. Pan, Z. Kang, S.T. Lee, New J. Chem. **35**, 2666 (2011)
15. A. Muthuvel, M. Jothibas, C. Manoharan, Nanotechnol. Environ. Eng. **5**, 1 (2020)
16. S.S. Sana, L.K. Dogiparthi, Mater. Lett. **226**, 47 (2018)
17. Y. Wang, A. Hu, J. Mater. Chem. C Mater. **2**, 6921 (2014)
18. S. Anwar, H. Ding, M. Xu, X. Hu, Z. Li, J. Wang, L. Liu, L. Jiang, D. Wang, C. Dong, M. Yan, Q. Wang, H. Bi, ACS Appl. Bio Mater. **2**, 2317 (2019)
19. S.Y. Lim, W. Shen, Z. Gao, Chem. Soc. Rev. **44**, 362 (2014)
20. M.X. Gao, C.F. Liu, Z.L. Wu, Q.L. Zeng, X.X. Yang, W.B. Wu, Y.F. Li, C.Z. Huang, Chem. Commun. **49**, 8015 (2013)
21. L. Tang, R. Ji, X. Cao, J. Lin, H. Jiang, X. Li, K.S. Teng, C.M. Luk, S. Zeng, J. Hao, S.P. Lau, ACS Nano **6**, 5102 (2012)
22. Z. Zhang, J. Chen, Y. Duan, W. Liu, D. Li, Z. Yan, K. Yang, Luminescence **33**, 318 (2018)
23. C. Cheng, Y. Shi, M. Li, M. Xing, Q. Wu, Mater. Sci. Eng. C **79**, 473 (2017)
24. G. Wu, M. Feng, H. Zhan, RSC Adv. **5**, 44636 (2015)
25. E.E. Ateia, A.T. Mohamed, M. Morsy, *Metal Oxide-Carbon Hybrid Materials: Synthesis, Properties and Applications* (2022), p. 103
26. M. Nagaraj, S. Ramalingam, C. Murugan, S. Aldawood, J.O. Jin, I. Choi, M. Kim, Environ. Res. **212**, 113273 (2022)
27. B. De, N. Karak, RSC Adv. **3**, 8286 (2013)
28. R. Sun, S. Liu, <https://doi.org/10.1080/21691401.2019.1593855> **47**, 1321 (2019)
29. Y.G. Denisenko, M.S. Molokeev, A.S. Oreshonkov, A.S. Krylov, A.S. Aleksandrovsky, N.O. Azarapin, O.V. Andreev, I.A. Razumkova, V.V. Atuchin, Crystals (Basel) **11**, 1027 (2021)
30. A.R. Nallayagari, E. Sgreccia, R. Pizzoferrato, M. Cabibbo, S. Kaciulis, E. Bolli, L. Pasquini, P. Knauth, M.L. Di Vona, J Nanostruct. Chem **12**, 565 (2022)
31. S. Sailaja Prasannakumaran Nair, N. Kottam, P.K. SG, J. Fluoresc. **30**, 357 (2020)

32. S. Shen, J. Wang, Z. Wu, Z. Du, Z. Tang, J. Yang, *Nanomaterials* **2020**(10), 375 (2020)
33. A.F. Shaikh, M.S. Tamboli, R.H. Patil, A. Bhan, J.D. Ambekar, B.B. Kale, J. *Nanosci. Nanotechnol.* **19**, 2339 (2018)
34. Y.N. Zhuravlev, V.V. Atuchin, *Nanomaterials* **10**, 10 (2020)
35. S. Shishodia, V. Rimal, P.K. Srivastava, *Appl. Nanosci.* **11**, 1691 (2021)
36. A. Kolanowska, G. Dzido, M. Krzywiecki, M.M. Tomczyk, D. Łukowiec, S. Ruczka, S. Boncel, *ACS Omega* **7**, 41165 (2022)
37. S. Qiang, L. Zhang, Z. Li, J. Liang, P. Li, J. Song, K. Guo, Z. Wang, Q. Fan, *Antioxidants* **11**, 2475 (2022)
38. S. Starikova, C. Jones, W.R. Forman, M. James Jee, J. Anthony Tyson, M.D. Schneider, T.G.F. Souza, V.S.T. Ciminelli, N.D.S. Mohallem, *J. Phys. Conf. Ser.* **733**, 012039 (2016)
39. U. Sivasankaran, S. Jesny, A.R. Jose, K. Girish Kumar, *Analyt. Sci.* **33**, 281 (2017)
40. J.D. Clogston, A.K. Patri, *Methods Mol. Biol.* **697**, 63 (2011)
41. H. Nie, M. Li, Q. Li, S. Liang, Y. Tan, L. Sheng, W. Shi, S.X.A. Zhang, *Chem. Mater.* **26**, 3104 (2014)
42. S. Hu, A. Trinchì, P. Atkin, I. Cole, *Angew. Chem. Int. Ed.* **54**, 2970 (2015)
43. Z.H. Wen, X.B. Yin, *RSC Adv.* **6**, 27829 (2016)
44. M. Sudolská, M. Dubecký, S. Sarkar, C.J. Reckmeier, R. Zbořil, A.L. Rogach, M. Otyepka, *J. Phys. Chem. C* **119**, 13369 (2015)
45. X. Miao, D. Qu, D. Yang, B. Nie, Y. Zhao, H. Fan, Z. Sun, X. Miao, D. Qu, D. Yang, B. Nie, Y. Zhao, Z. Sun, Y. Zhao Beijing Guangqumen High School, H. Fan, *Advanced Materials* **30**, 1704740 (2018)
46. A. Visheratina, L. Hesami, A.K. Wilson, N. Baalbaki, N. Noginova, M.A. Noginov, N.A. Kotov, *Chirality* **34**, 1503 (2022)
47. S.-S. Hsiao, P.-H. Wang, N.-T. Nguyen, T.-T. Le, C.-K. Chen, S.-S. Chen, C.-T. Chang, *J. Nanosci. Nanotechnol.* **21**, 1653 (2021)
48. S. Kundu, R.M. Yadav, T.N. Narayanan, M.V. Shelke, R. Vajtai, P.M. Ajayan, V.K. Pillai, *Nanoscale* **7**, 11515 (2015)
49. M. Saleh Mohammadnia, H. Roghani-Mamaqani, H. Mardani, A. Rezvani-Moghaddam, S. Hemmati, M. Salami-Kalajahi, *Carbohydr. Polym.* **294**, 119768 (2022)
50. A. Tyagi, K.M. Tripathi, N. Singh, S. Choudhary, R.K. Gupta, *RSC Adv.* **6**, 72423 (2016)
51. J. Yu, C. Liu, K. Yuan, Z. Lu, Y. Cheng, L. Li, X. Zhang, P. Jin, F. Meng, H. Liu, *Nanomaterials* **8**, 233 (2018)
52. L. Bao, C. Liu, Z.-L. Zhang, D.-W. Pang, L. Bao, C. Liu, Z. Zhang, D. Pang, *Adv. Mater.* **27**, 1663 (2015)
53. S.D. Souza, M. Buerkle, P. Brunet, C. Maddi, D.B. Padmanaban, A. Morelli, A.F. Payam, P. Maguire, D. Mariotti, V. Svrcek, *Carbon N Y* **183**, 1 (2021)
54. R.H. Bube, *Proc. IRE* **43**, 1836 (1955)
55. D.G. Barton, M. Shtein, R.D. Wilson, S.L. Soled, E. Iglesia, *J. Phys. Chem. B* **103**, 630 (1999)
56. L. Ma, Z. Xia, V. Atuchin, M. Molokeev, S. Auluck, A.H. Reshak, Q. Liu, *Phys. Chem. Chem. Phys.* **17**, 31188 (2015)
57. N.O. Azarapin, N.A. Khritokhin, V.V. Atuchin, A.A. Gubin, M.S. Molokeev, S. Mukherjee, O.V. Andreev, *Crystals (Basel)* **13**, 903 (2023)
58. M.E. Khan, A. Mohammad, T. Yoon, *Chemosphere* **302**, 134815 (2022)
59. J.A. Yan, L. Xian, M.Y. Chou, *Phys. Rev. Lett.* **103**, 086802 (2009)
60. C.-T. Chien, S.-S. Li, W.-J. Lai, Y.-C. Yeh, H.-A. Chen, I.-S. Chen, L.-C. Chen, K.-H. Chen, T. Nemoto, S. Isoda, M. Chen, T. Fujita, G. Eda, H. Yamaguchi, M. Chhowalla, C.-W. Chen, *Angew. Chem.* **124**, 6766 (2012)
61. Z. Li, Y. Zhang, Q. Niu, M. Mou, Y. Wu, X. Liu, Z. Yan, S. Liao, *J. Lumin.* **187**, 274 (2017)
62. H. Ding, Y. Ji, J.S. Wei, Q.Y. Gao, Z.Y. Zhou, H.M. Xiong, *J Mater Chem B* **5**, 5272 (2017)
63. Y. Xu, C.J. Tang, H. Huang, C.Q. Sun, Y.K. Zhang, Q.F. Ye, A.J. Wang, *Chin. J. Anal. Chem.* **42**, 1252 (2014)
64. R. Atchudan, T.N. Jebakumar Immanuel Edison, M. Shanmugam, S. Perumal, T. Somanathan, Y.R. Lee, *Phys. E Low Dimens. Syst. Nanostruct.* **126**, 114417 (2021)
65. X. Jia, J. Li, E. Wang, *Nanoscale* **4**, 5572 (2012)
66. Y. Dong, R. Wang, H. Li, J. Shao, Y. Chi, X. Lin, G. Chen, *Carbon N Y* **50**, 2810 (2012)
67. S. Samimi, M.S. Ardestani, F.A. Dorkoosh, *J. Drug Deliv. Sci. Technol.* **61**, 102287 (2021)